




# Construction of Ni–Mo–P heterostructures with efficient hydrogen evolution performance under acidic condition

Tian-Yun Chen<sup>1,2</sup>, Ya-Qi Zhang<sup>1,2</sup>, Ying-Yan Fu<sup>1,2</sup>, Min Qian<sup>1,2</sup>, Hao-Jiang Dai<sup>1,2</sup>, Bo Ye<sup>1,2</sup>, Shan Qin<sup>1,2</sup>, and Qing-Hua Yang<sup>1,2,\*</sup> 

<sup>1</sup>School of Chemistry and Chemical Engineering, Hefei University of Technology, Hefei 230009, Anhui, China

<sup>2</sup>School of Food and Biological Engineering, Hefei University of Technology, Hefei 230009, Anhui, China

Received: 12 March 2021

Accepted: 21 April 2021

Published online:  
6 May 2021

© The Author(s), under exclusive licence to Springer Science+Business Media, LLC, part of Springer Nature 2021

## ABSTRACT

Hydrogen energy is regarded as one of the most important clean energy in the twenty-first century, and improving the catalytic efficiency of hydrogen evolution reaction (HER) is the basis for realizing the large-scale hydrogen production. Transition metal phosphides (TMPs) were proved to be efficient electrocatalysts for HER. In this work, we first synthesized the nickel-molybdenum bimetallic precursors, followed by high-temperature calcination in air. Finally, NiMoP/MoP nanorods (Ni–Mo–P NRs) was obtained by chemical vapor deposition (CVD) of phosphating. The target catalyst of Ni–Mo–P NRs was characterized by transmission electron microscopy (TEM), scanning electron microscopy (SEM), X-ray diffraction (XRD) and X-ray photoelectron spectroscopy (XPS). For Ni–Mo–P NRs, the electrochemical test in 0.5 M H<sub>2</sub>SO<sub>4</sub> solution for HER showed that the optimal feeding ratio was Ni:Mo = 1:1. And the Ni<sub>1</sub>–Mo<sub>1</sub>–P NRs presented an onset potential of 63.2 mV, and an overpotential of 117.9 mV was required to drive the current density of 10 mA cm<sup>-2</sup>. Meanwhile, The Tafel slope, exchange current density (*j*<sub>0</sub>), electrochemical double-layer capacitance (*C*<sub>dl</sub>) were 58.6 mV dec<sup>-1</sup>, 0.10 mA cm<sup>-2</sup>, 12.6 mF cm<sup>-2</sup>, respectively. Moreover, there was no obvious activity diminish of Ni<sub>1</sub>–Mo<sub>1</sub>–P NRs after a long-term stability and durability test.

## 1 Introduction

In the past few years, as the society developed rapidly and the fast consumption of traditional fossil fuels, the energy crisis and ecological environment

problems caused by them have attracted great attention, which forces people to seek an ideal renewable energy source [1–4]. As a desirable clean energy, energy density of hydrogen can reach up to 120–140 MJ kg<sup>-1</sup> [5]. And HER is a half reaction of water electrolysis, which has no pollution to the

Address correspondence to E-mail: yqhsina@hfut.edu.cn

environment. However, in view of the low efficiency of HER process and the large overpotential caused by slow kinetic processes, an efficient catalyst capable of overcoming the energy barrier is needed to accelerate the reaction rate [6–8]. Commercial Pt-based catalysts are recognized as the catalysts with best performance so far, but their high price and instability in strong acid or alkaline medium limit the industrialization of hydrogen production [9, 10]. Inexpensive, high-efficiency and steady-going electrocatalysts need to be explored urgently.

Ideal electrocatalysts should not only have more exposed active sites and excellent conductivity, but also have special surface structures that facilitate rapid removal of hydrogen ( $H_2$ ), such as nanorods, nano-polyhedrons, nanotubes [11–13]. In addition, researchers have currently explored a range of transition metal catalysts, for example, carbides (TMCs), nitrides (TMNs), sulfides (TMSs), phosphides (TMPs) for HER. Among them, TMPs like FeP [14, 15],  $Ni_2P$  [16, 17], CoP [18, 19], were deemed to be promising electrocatalysts since its catalytic mechanism is analogous to that of hydrogenase. In addition, P in TMPs can be used as a proton receptor center to promote the formation of transition metal hydrides, thus promoting the subsequent electrochemical desorption process. Furthermore, TMPs have better stability under extreme conditions.

Lately, molybdenum (Mo) phosphides were expected to replace precious metals catalysts for hydrogen evolution reaction because of their low-cost, high activity and strong durability [20–22]. Yang et al. used the MOF to synthesize MoP@PC showed excellent catalytic activity toward HER. The overpotential of 153 mV were needed to drive a current density of  $10 \text{ mA cm}^{-2}$  and the Tafel slope was  $66 \text{ mV dec}^{-1}$  [23]. Besides,  $Ni_2P$  was regarded as a highly active catalyst since it was familiar with the catalytic mechanism of ferronickel hydrogenase and has been widely studied among TMPs in recent years [24, 25]. In addition, studies have shown that bimetallic TMPs such as Fe–Co–P [26, 27], Fe–Ni–P [28–30], Ni–Co–P [31–33] exhibited good HER or OER activity due to the synergistic effect between bimetals, which enhanced the conductivity, optimized the reaction adsorption energy and reduced the reaction energy barrier in the catalytic process. Moreover, the reasonable design of hybrid architecture is also a significant method to optimize HER activity [34].

Based on the analysis above, we designed and synthesized heterogeneous  $Ni_x\text{--}Mo_y\text{--}P$  NRs ( $x, y$  represented the molar ratio of Ni to Mo) by a simple and efficient three-step method. Electrochemical measurements under acidic conditions for HER showed that  $Ni_1\text{--}Mo_1\text{--}P$  NRs had the best activity with an onset potential ( $\eta_0$ ) of 63.2 mV, Tafel slope of  $58.6 \text{ mV dec}^{-1}$ , an overpotential of 117.9 mV at  $10 \text{ mA cm}^{-2}$ , respectively. Furthermore,  $Ni_1\text{--}Mo_1\text{--}P$  NRs maintained the activity and morphology well even after long-term stability test.

## 2 Experimental

### 2.1 Materials

Nickel chloride hexahydrate ( $NiCl_2 \cdot 6H_2O$ , AR), ammonium molybdate tetrahydrate ( $(NH_4)_6\text{--}Mo_7O_{24} \cdot 4H_2O$ , AR), urea ( $CO(NH_2)_2$ , AR) and diammonium hydrogen phosphate ( $(NH_4)_2HPO_4$ , AR) were all purchased from Aladdin Industrial Corporation (Shanghai, China). All chemical reagents were used without further purification.

### 2.2 Preparation of catalysts

#### 2.2.1 Preparation of $Ni_xMo_y$ precursor

Preparation of  $Ni_1Mo_1$  precursor referred to the literature with slight modification [35]. Solution A:  $NiCl_2 \cdot 6H_2O$  (1 mmol, 0.238 g) and urea (5 mmol, 0.3 g) dissolved in 30 mL deionized water and stirred vigorously; Solution B:  $(NH_4)_2Mo_7O_{24} \cdot 6H_2O$  (1 mmol, 1.235 g) was completely dissolved in 30 mL deionized water; Solution C: solution B was added to solution A dropwise under strong magnetic stirring. The solution C was transferred to a 100 mL Teflon-lined stainless-steel autoclave and reacted at  $160 \text{ }^\circ\text{C}$  for 16 h. After cooling down to ambient temperature, the product was collected by centrifugation and washed with deionized water and absolute ethanol for several times, and then dried at  $60 \text{ }^\circ\text{C}$  in oven for 12 h. The control experiment adjusted the molar ratio of Ni to Mo ( $x:y = 1:0, 1:2, 2:1$ ) under the same condition.

### 2.2.2 Preparation of $Ni_x-Mo_y-O$ NRs

Put an appropriate amount of  $Ni_xMo_y$  precursor in a porcelain boat and subjected to 400 °C treatment under air for 3 h under air with a temperature ramping rate of 5 °C min<sup>-1</sup>. Take it out after cooling down to room temperature for further use.

### 2.2.3 Preparation of $Ni_x-Mo_y-P$ NRs

$(NH_4)_2HPO_4$  as phosphorus source and  $Ni_x-Mo_y-O$  NRs were placed separately in a porcelain boat followed by introducing 10%  $H_2/Ar$ , then heated to 850 °C and maintained for 2 h with a temperature ramping rate of 5 °C min<sup>-1</sup>. After the reaction, the catalyst was cooled to room temperature and taken out for electrochemical performance testing.

## 2.3 Characterization

The surface morphology, structure and chemical composition of the samples were characterized by TEM (JEM-1400F, JEOL, Japan) with energy dispersive X-ray spectrum (EDS), XRD (Rigaku MiniFlex-600) with a Cu radiation source ( $\lambda = 0.1540$  nm), SEM (SU8020, Hitachi, Japan), XPS ((ESCALAB250Xi, Thermo, United States), respectively.

## 2.4 Electrochemical test

All electrochemical tests were performed in a three-electrode system at room temperature on an electrochemical workstation of CHI760 with an electrolyte of 0.5 M  $H_2SO_4$  solution saturated with  $N_2$ . The glassy carbon electrode (GCE, area is 0.196 cm<sup>2</sup>) was used as the working electrode, while the Ag/AgCl electrode was used as the reference electrode and the carbon rod was used as the counter electrode. Firstly, 5 mg of the prepared catalyst was evenly dispersed in 1 mL of mixed solvent of absolute ethanol and Nafion (volume ratio: 19:1) by ultrasonicated for 0.5 h. Then a proper amount of well-dispersed catalyst solution was dropwise added onto the glassy carbon electrode with a pipette, and the test was conducted after natural drying. The scanning rate for the linear sweep voltammetry (LSV) test was 5 mV s<sup>-1</sup>. The cyclic voltammetry (CV) scan rate for stability and durability was 50 mV s<sup>-1</sup>. Electrochemical impedance spectroscopy (EIS) measurement was carried out with a frequency range from

100 kHz to 0.1 Hz at an amplitude of 5 mV. All potentials were corrected for standard hydrogen electrode potential according to the equation  $E$  (vs. RHE) =  $E$  (vs. Ag/AgCl) + 0.197 + 0.059pH.

## 3 Results and discussion

In this work, firstly, ammonium molybdate solution was added dropwise into the solution of nickel nitrate and urea to synthesize precursors of  $Ni_xMo_y$  bimetallic nanorods with different molar ratios of  $NiCl_2 \cdot 6H_2O$  to  $(NH_4)_6Mo_7O_{24} \cdot 4H_2O$  through simple hydrothermal reaction, and the color of the precursor gradually became lighter with the increase of Mo content. Then, the precursors were calcined into  $Ni_x-Mo_y-O$  NRs at high temperature in air. Finally,  $Ni_x-Mo_y-P$  NRs was obtained by CVD phosphating process. The detailed synthesis process was shown in Fig. 1.

It can be found that in the absence of ammonium molybdate, the synthesized nickel precursor was a very thin nanowire, and its morphology was usually difficult to maintain at high temperature (Figs. S1b, S3a). The nano-particles of NiO (PDF NO.41-1049) were formed by high-temperature calcination (Figs. S4, S5b). When Ni:Mo ratio reached 1:1 and 2:1, the morphology of the as-prepared  $Ni_xMo_y$  are nanorods with smooth surface, but the size reached about 200 nm (Figs. S1a, d, S3b, d), and the XRD patterns are almost identical (Fig.S2). After pyrolysis in air, the XRD peaks at 14.3°, 24.0°, 29.8°, 33.3° and 44.1° were consistent with  $NiMoO_4$  (PDF No. 86-0361) (Fig. S4), and Figure S5a,d indicated good morphology. It should be noted that when the NiMo ratio was 1:2, black particles (Fig. S1c) emerged on the surface of the  $Ni_1Mo_2$  precursor and it was likely that the excessive Mo species caused slight changes in the crystal structure and morphology. Besides, the diffraction peaks of  $MoO_3$  (PDF NO. 05-0508) appeared in XRD pattern after pyrolysis in addition to  $NiMoO_4$  (Fig. S4), and the morphology remained good after high-temperature calcination (Fig. S5c).

After  $Ni_x-Mo_y-O$  was phosphated by CVD method,  $Ni_2P$  (PDF NO. 03-0953) nanoparticles was obtained when the molar ratio of Ni to Mo was 1:0 (Figs. 2, 3a).  $NiMo$  bimetallic oxide was converted into  $Ni_x-Mo_y-P$  dendritic nanorods (Fig. 3b–d), and the diffraction peaks at 30.5°, 35.3°, 39.2°, 47.3°, 49.2°, 58.9° correspond to the (110), (200), (111), (210), (002),

**Fig. 1** Schematic illustration of synthesis procedure for  $Ni_x-Mo_y-P$  hierarchical nanorods

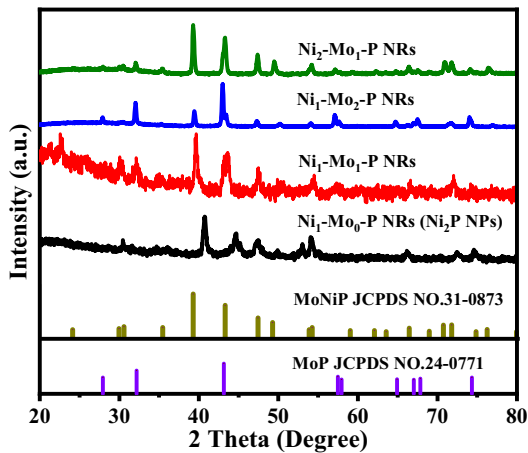
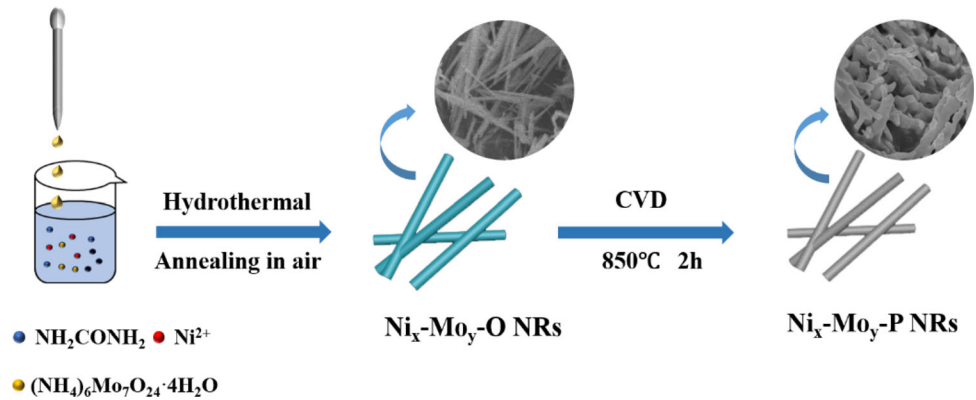


**Fig. 2** XRD patterns of a  $Ni_x-Mo_y-P$  NRs

(112) planes of NiMoP (PDF NO. 31-0873), while diffraction peaks at  $27.9^\circ$ ,  $32.2^\circ$ ,  $43.1^\circ$ ,  $57.5^\circ$ ,  $58.0^\circ$  and  $67.9^\circ$  perfectly corresponded to the (001), (100), (101), (110), (002) and (102) planes of MoP (PDF NO. 24-0771) (Fig. 2). With the increasing of Mo content, the peaks intensity of MoP strengthened while the peaks of NiMoP decreased gradually. Additionally, SEM images of  $Ni_x-Mo_y-P$  NRs (Fig. 4a–d) indicated that the rod-like structure were well maintained. As revealed by high-resolution TEM (HRTEM) images (Fig. 3e) of  $Ni_1-Mo_1-P$  NRs, the lattice fringes with interplanar spacing of 0.255 nm belonged to the (200) facet of MoNiP while the characteristic lattice spacing of 0.159 nm was ascribed to (002) of MoP. Besides, it

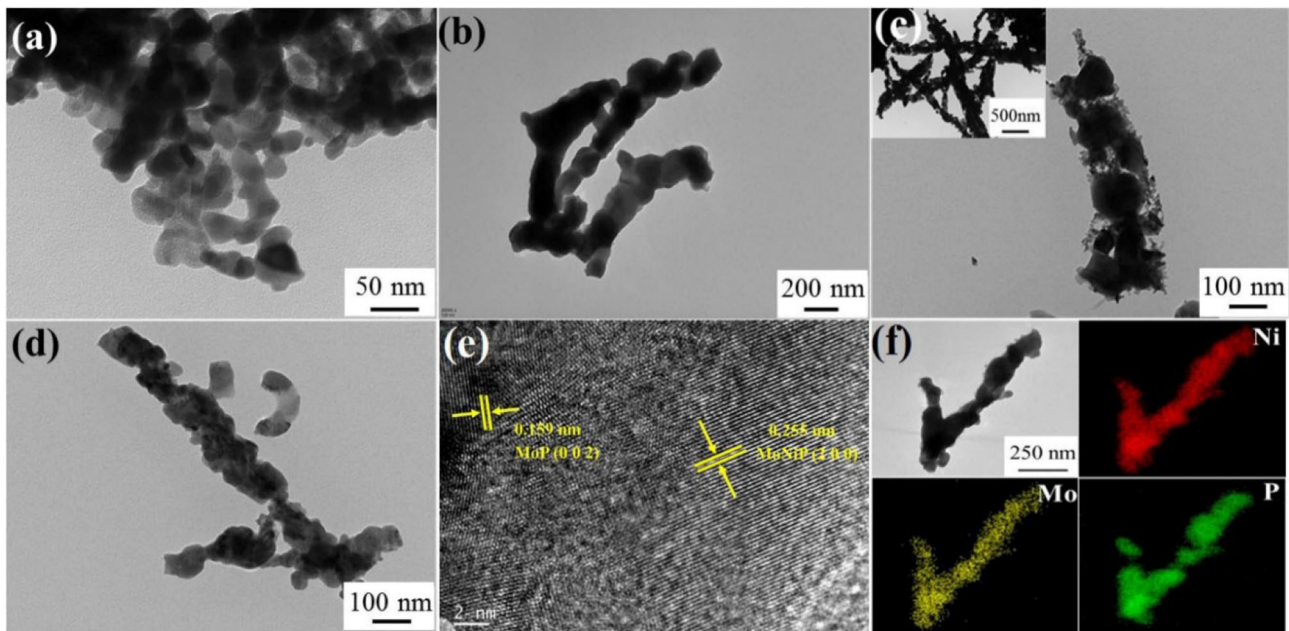
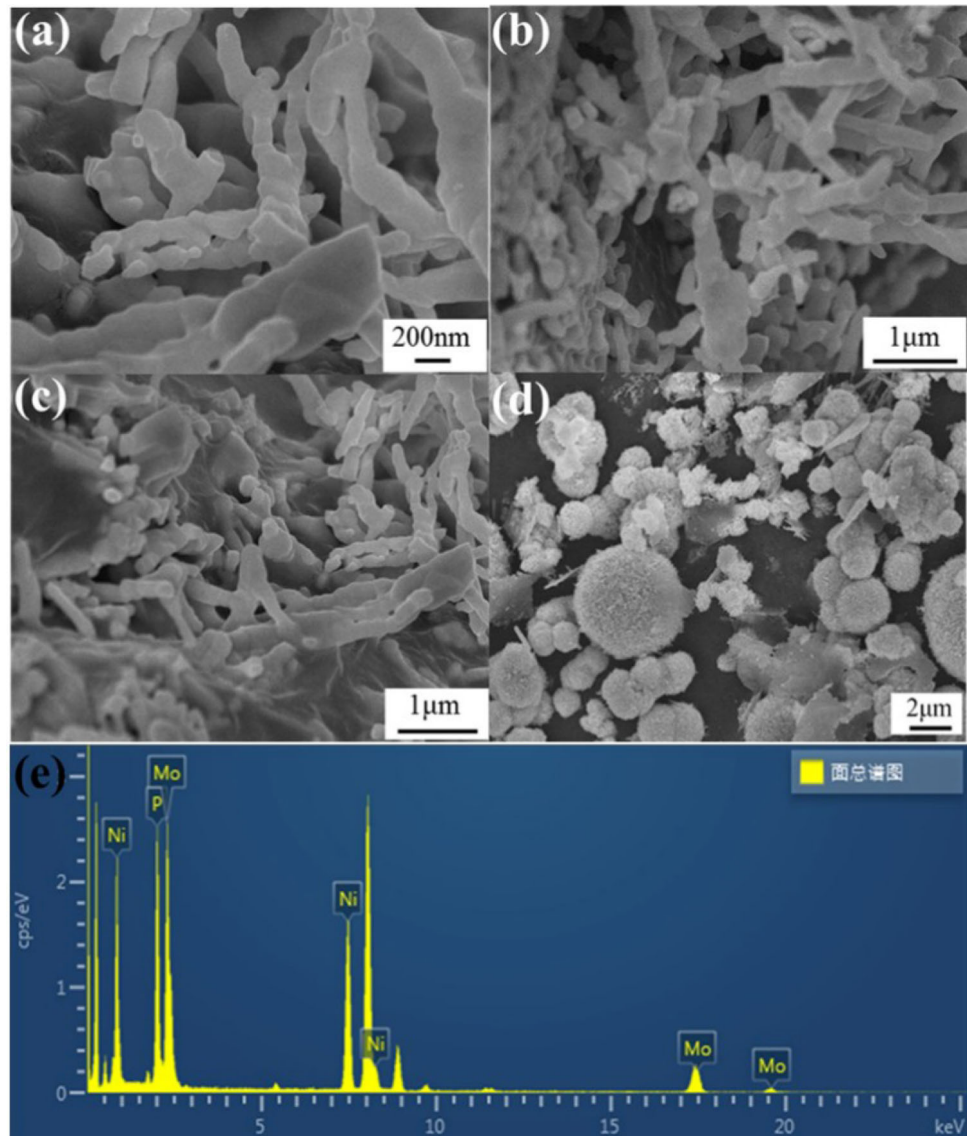


**Fig. 3** TEM images a–d of  $Ni_1-Mo_0-P$  NPs,  $Ni_1-Mo_1-P$ ,  $Ni_1-Mo_2-P$ ,  $Ni_2-Mo_1-P$  NRs, e high-resolution TEM images of the  $Ni_1-Mo_1-P$  NRs, f TEM image of  $Ni_1-Mo_1-P$  NRs and corresponding elemental mapping images



**Fig. 4** SEM images of **a** Ni<sub>1</sub>-Mo<sub>1</sub>-P NPs, **b** Ni<sub>1</sub>-Mo<sub>2</sub>-P NRs, **c** Ni<sub>2</sub>-Mo<sub>1</sub>-P NRs, **d** Ni<sub>1</sub>-Mo<sub>0</sub>-P NPs, **e** EDS spectra of Ni<sub>1</sub>-Mo<sub>1</sub>-P NRs



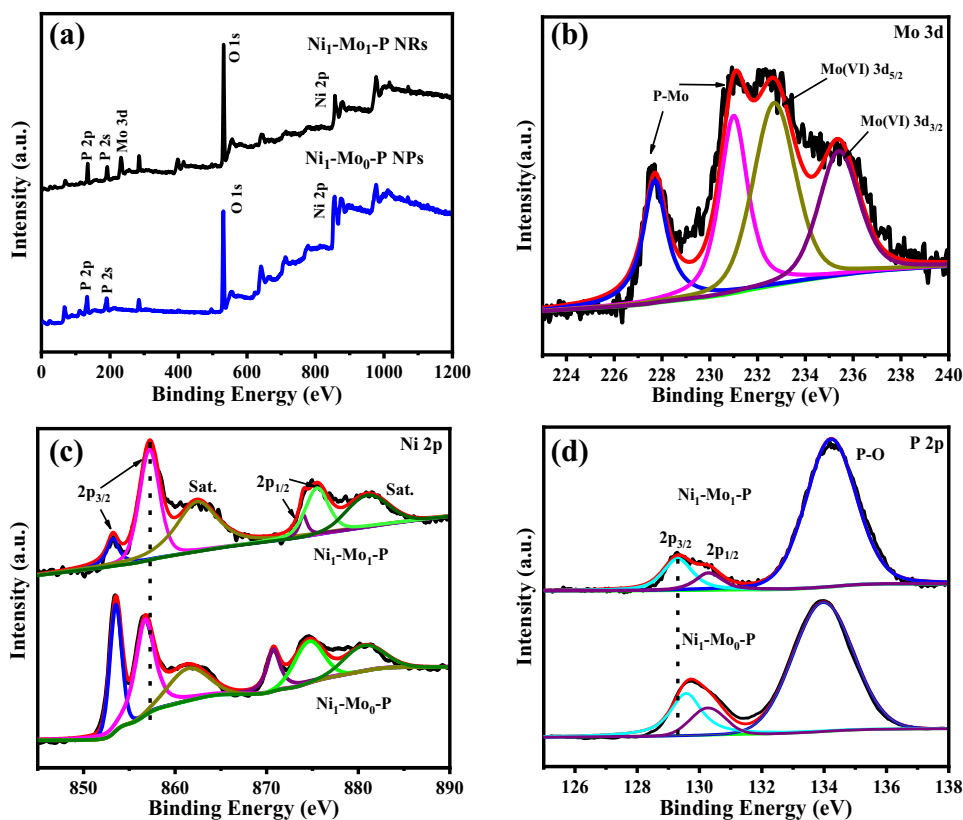
can be known that the elements of Ni, Mo and P were distributed uniformly on the surface of Ni<sub>1</sub>-Mo<sub>1</sub>-P NRs (Fig. 3f), and corresponding atomic ratio was 40.27:30.94:28.80 (Table 1). The optimum ratio of nickel and molybdenum metal atoms facilitates crystal growth in a particular lattice plane. Table S1 listed the atomic percentage of Ni, Mo and P in Ni<sub>x</sub>-Mo<sub>y</sub>-P NRs.

**Table 1** The weight and atomic percentage of different elements in Ni<sub>1</sub>-Mo<sub>1</sub>-P NRs

Elements	wt%	at%
P	21.41	40.27
Ni	31.17	30.93
Mo	47.42	28.80
Total	100.00	100.00

To further determine the elemental content and valence state of Ni<sub>1</sub>-Mo<sub>1</sub>-P NRs, XPS measurement was executed. The existence of Ni, Mo, P, O was confirmed by the XPS full spectrum of Ni<sub>1</sub>-Mo<sub>1</sub>-P NRs (Fig. 5a), which was consistent with EDS results (Fig. 4e). In the high-resolution XPS spectra of Mo 3d (Fig. 5b), the two peaks at the binding energies (BE) of 227.8 eV and 231.1 eV can be attributed to the metal phosphide Mo-P, and the doublets at 232.48 eV and 235.38 eV corresponded to the oxidation state of Mo due to the higher surface energy of MoP [36–38]. In the region of Ni 2p (Fig. 5c), it should be noted that the peaks at 853.1 eV and 873.9 eV could be assigned to Ni 2p<sub>3/2</sub> and Ni 2p<sub>1/2</sub> in Ni-P which had a positive shift compared with that of Ni<sub>1</sub>-Mo<sub>0</sub>-P NPs because

**Fig. 5** XPS spectra of the Ni<sub>1</sub>-Mo<sub>1</sub>-P NRs and Ni<sub>1</sub>-Mo<sub>0</sub>-P NPs **a** survey, **b** Mo 3d, **c** Ni 2p, **d** P 2p



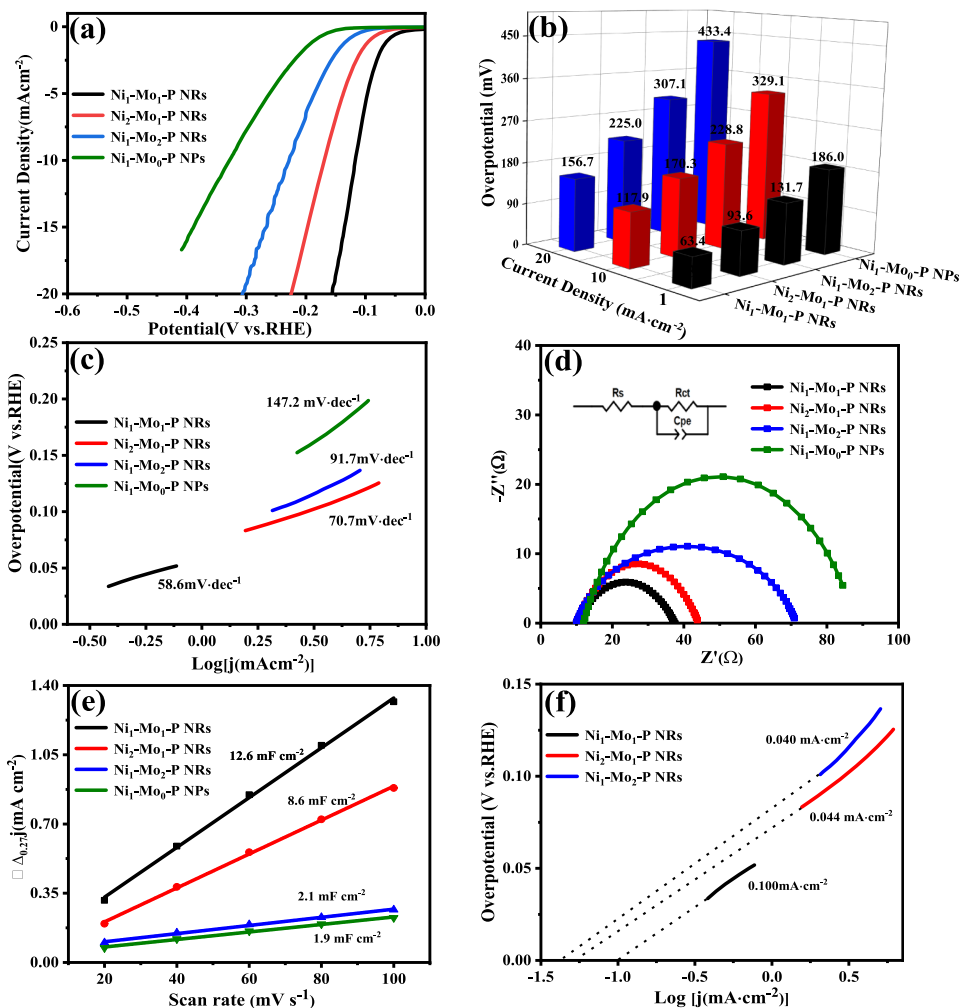
of the electronegativity difference between Ni (1.91) and Mo (2.16) [17, 22]. The doublets at 857.1 eV and 875.33 eV could be ascribed to the oxidation state of Ni species because of passivation in air while two peaks at 862.4 eV and 880.8 eV were satellite peaks [39, 40]. For P 2p spectra (Fig. 5d), characteristic peaks located at 129.3 eV and 130.3 eV were designated to metal phosphide (P 2p<sub>3/2</sub> and 2p<sub>1/2</sub>) [18], which showed mildly negative offset compared to P 2p in Ni<sub>1</sub>-Mo<sub>0</sub>-P NPs. Furthermore, the broad peak near 134.2 eV was attributed to oxidized P substances such as phosphates and phosphorus pentoxide [9, 15]. It is observed that nickel has a partial positive charge ( $\delta^+$ ) while phosphorus had a partial negative charge ( $\delta^-$ ), which indicated that the electron was transferred from metal element to phosphorus element. These phenomena mean that the addition of Mo result in the charge redistribution in catalysts and reduce the energy barrier of the electrocatalytic process, which promoted the adsorption and dissociation process of water in HER [41, 42].

The electrocatalytic properties of the Ni<sub>1</sub>-Mo<sub>1</sub>-P NRs towards HER was investigated by the linear sweep voltammetry (LSV) using a standard three-electrode electrochemical cell in 0.5 M H<sub>2</sub>SO<sub>4</sub>

solution saturated by N<sub>2</sub>. The control samples of Ni<sub>2</sub>-Mo<sub>1</sub>-P NRs, Ni<sub>1</sub>-Mo<sub>2</sub>-P NRs, Ni<sub>1</sub>-Mo<sub>0</sub>-P NPs electrodes were also studied under the same conditions for comparison. As shown in LSV curves (Fig. 6a), the Ni<sub>1</sub>-Mo<sub>1</sub>-P NRs exhibited promising HER performance with an ultrasmall onset potential of 63.4 mV and an overpotential of 117.9 mV at a current density of 10 mA cm<sup>-2</sup>, which was much lower than those of Ni<sub>2</sub>-Mo<sub>1</sub>-P NRs (170.3 mV), Ni<sub>1</sub>-Mo<sub>2</sub>-P NRs (228.8 mV), and Ni<sub>1</sub>-Mo<sub>0</sub>-P NPs (329.1 mV), suggesting that Ni<sub>1</sub>-Mo<sub>1</sub>-P NRs had high activity toward HER in acidic electrolyte. To display the outstanding catalytic activity of Ni<sub>x</sub>-Mo<sub>y</sub>-P NRs, the required overpotentials of as-prepared catalysts at different current density of 1, 10, 20 mA cm<sup>-2</sup> were presented in Fig. 6b.

The Tafel slope was calculated from the LSV curve based on Tafel equation:  $\eta = b \lg j + a$  ( $b$ ,  $j$  represented Tafel slope and current density), and comparisons of Tafel slopes were demonstrated in Fig. 6c. The Tafel slope of Ni<sub>1</sub>-Mo<sub>1</sub>-P NRs was 58.6 mV dec<sup>-1</sup>, which was smaller than that of Ni<sub>2</sub>-Mo<sub>1</sub>-P (70.7 mV dec<sup>-1</sup>), Ni<sub>1</sub>-Mo<sub>2</sub>-P (91.7 mV dec<sup>-1</sup>) and Ni<sub>1</sub>-Mo<sub>0</sub>-P (147.2 mV dec<sup>-1</sup>), indicating faster kinetics of Ni<sub>1</sub>-Mo<sub>1</sub>-P NRs in HER. Typically, H<sub>2</sub>

**Fig. 6** **a** LSV curves, **b**  $\eta_1$ ,  $\eta_{10}$  and  $\eta_{20}$ , **c** corresponding tafel slopes, **d** EIS Nyquist plots; **e**  $C_{dl}$  at 0.26 V as a function of scan rates and **f**  $j_0$  of different catalysts in 0.5 M  $H_2SO_4$  solution



production involves two different reaction pathways, namely, Volmer–Heyrovsky and Volmer–Tafel mechanisms, as determined by the change of Tafel slope [43]. Theoretically, the Tafel slopes corresponding to Volmer, Heyrovsky and Tafel processes are 120, 40 and 30  $mV\ dec^{-1}$ , respectively [44].  $Ni_1-Mo_1-P$  NRs manifested the Tafel slopes of 58.6  $mV\ dec^{-1}$ , suggesting a Volmer–Heyrovsky mechanism for  $Ni_1-Mo_1-P$  NRs and the Heyrovsky process was the rate-limiting step.

Furthermore, the electrochemical impedance spectroscopy (EIS) was measured to further explore the HER kinetics of  $Ni_1-Mo_1-P$  NRs. The equivalent circuit diagram embedded in Fig. 6d, where  $R_s$ , CPE,  $R_{ct}$  stands for the solution resistance, constant-phase element, and charge-transfer resistance, respectively [45, 46]. The semicircle diameter represents the charge transfer resistances ( $R_{ct}$ ), which can evaluate the charge transfer capability. The measured  $R_{ct}$  of

$Ni_1-Mo_1-P$  NRs was 28.4  $\Omega$  was lower than  $Ni_2-Mo_1-P$  NRs (33.8  $\Omega$ ),  $Ni_1-Mo_2-P$  NRs (60.9  $\Omega$ ) and  $Ni_1-Mo_0-P$  NPs (72.2  $\Omega$ ), owing to its ample synergetic interfaces that benefits the integration of electrons and reactants at the catalyst-electrolyte interphase and short diffusion [47, 48].

To investigate the intrinsic activity of materials, the electrochemical surface areas (ECSA) of the catalysts were also studied by testing the double layer capacitance ( $C_{dl}$ ) at varied scan rates. The CV curves for  $Ni_1-Mo_1-P$  NRs,  $Ni_2-Mo_1-P$  NRs,  $Ni_1-Mo_2-P$  NRs and  $Ni_1-Mo_0-P$  NPs (Fig. S6) within 0.05–0.45 V at different scanning rates of 10–100  $mV\ s^{-1}$  were performed. The  $C_{dl}$  was measured by plotting the difference between anode current ( $j_a$ ) and cathode current ( $j_c$ ) at a constant potential 0.26 V vs reversible hydrogen electrode (RHE) with respect to the scanning rates. As shown in Fig. 6e and Fig. S7,  $Ni_1-Mo_1-P$  NRs had the highest  $C_{dl}$  (12.6  $mF\ cm^{-2}$ ) and ECSA

(315 cm<sup>2</sup>) among all catalysts, which indicated that more active sites were exposed on the surface of Ni<sub>1</sub>–Mo<sub>1</sub>–P NRs to improve HER performance [49, 50].

The exchange current density (*j*<sub>0</sub>) is another important criterion for evaluating HER activity which can be obtained by extrapolation from Tafel slope diagram (Fig. 6f). The *j*<sub>0</sub> for Ni<sub>1</sub>–Mo<sub>1</sub>–P NRs was 0.10 mA cm<sup>-2</sup>, which was higher than other catalysts, further proving the excellent performance. Table 2 listed the performance comparison of several catalysts under acidic conditions in recent years.

In addition to the excellent catalytic performance, stability is an essential criterion for judging the quality of catalysts. Stability and durability test of Ni<sub>1</sub>–Mo<sub>1</sub>–P NRs were performed in 0.5 M H<sub>2</sub>SO<sub>4</sub> solution as shown in Fig. 7a. The current density decayed by 5.4 mV at a current density of 10

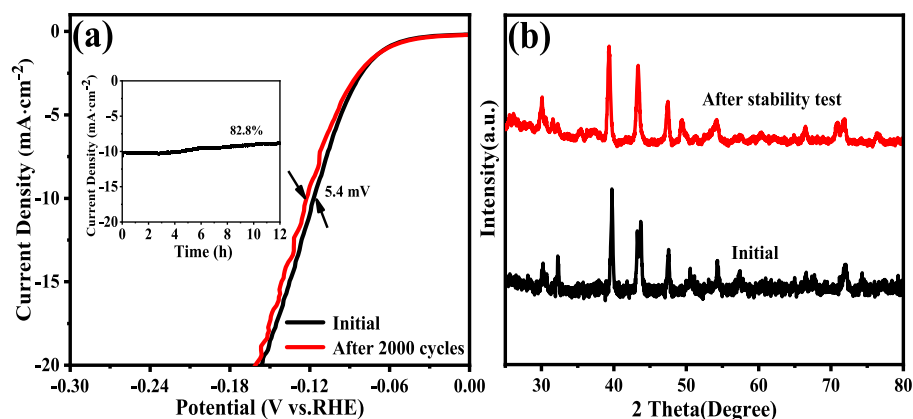
mA cm<sup>-2</sup> after continuously scanning for 2000 times using cyclic voltammetry. Meanwhile, the durability of Ni<sub>1</sub>–Mo<sub>1</sub>–P NRs was determined by a chronoamperometric curve, and the catalytic activity was maintained at 82.8% after 12 h of continuous testing. This indicated that Ni<sub>1</sub>–Mo<sub>1</sub>–P NRs has good stability and corrosion resistance. Moreover, according to the comparison of XRD patterns before and after the stability test (Fig. 7b), it was quite clear that the crystal structure of Ni<sub>1</sub>–Mo<sub>1</sub>–P NRs was almost unchanged, which also indicated better stability and durability of the target catalyst.

Excellent HER activity and stability can be attributed to the following aspects: (1) bimetallic phosphides can effectively improve the adsorption of hydrogen, and the incorporation of Mo can effectively change the charge distribution of Ni<sub>x</sub>–Mo<sub>y</sub>–P

**Table 2** Performance comparison of electrocatalysts for hydrogen evolution reaction under acidic conditions

Catalysts	$\eta_{10}$ (mV)	Tafel slope (mA dec <sup>-1</sup> )	References
N-MoP	173	54	[9]
FeP/C	110	57	[14]
CoP NTs	108	59	[19]
Fe <sub>0.01</sub> –MoP	195	49	[20]
MoP <sub>2</sub> NPs/Mo	143	57	[21]
MoP@PC	153	66	[23]
Ni–Co–P MFs	90	84	[32]
MoP/Fe <sub>2</sub> P/RGO	156	51	[34]
0.02Ni–MoP	102	58.1	[39]
CoP NSs/CC	49	30.1	[46]
FeP SS	66	45	[47]
CoP CNTs	139	52	
CoP-60	121	56	[50]
Ni <sub>1</sub> –Mo <sub>1</sub> –P NRs	117.9	58.6	This work

**Fig. 7** **a** stability test of Ni<sub>1</sub>–Mo<sub>1</sub>–P NRs in 0.5 M H<sub>2</sub>SO<sub>4</sub> solution, **b** Comparison of XRD patterns before and after electrolysis,





NRs; (2) Ni<sub>1</sub>-Mo<sub>1</sub>-P NRs has good conductivity, faster charge transfer kinetics and more active sites; (3) One-dimensional structure also contributes to excellent durability and long-term stability.

## 4 Conclusions

To sum up, Ni<sub>1</sub>-Mo<sub>1</sub>-P NRs with high performance for HER was prepared by simple hydrothermal method, high temperature calcination and CVD method in turn. The results showed that the addition of Mo optimized the electronic distribution of catalyst, and Ni<sub>1</sub>-Mo<sub>1</sub>-P NRs represented excellent HER activity with a small onset potential of 63.4 mV and super stability in acidic medium. This work provides a feasible strategy for preparing other transition metal phosphorus heterostructure electrocatalysts, which can realize steady and robust electrochemical hydrogen production. The abundant metal source, highly efficient and stable catalytic activity make Ni<sub>1</sub>-Mo<sub>1</sub>-P NRs become one of the potential catalysts for hydrogen production industrialization.

## Acknowledgements

This work was supported by Anhui Provincial Natural Science Foundation (Grant No. 1808085ME143) and the State Key Laboratory of Advanced Technology for Materials Synthesis and Processing (Grant No. 2021-KF-20, Wuhan University of Technology).

## Declarations

**Conflict of interest** The authors declare that they have no competitive economic interests or personal relationships, which could affect the work reported in this paper.

**Supplementary Information:** The online version contains supplementary material available at <http://doi.org/10.1007/s10854-021-06048-5>.

## References

- C.G. Morales-Guio, L.A. Stern, X. Hu, *Chem. Soc. Rev.* **43**, 6555–6569 (2014)
- B. Hua, M. Li, Y.F. Sun, Y.Q. Zhang, N. Yan, J. Chen, T. Thundat, J. Li, J.L. Luo, *Nano Energy* **32**, 247–254 (2017)
- H. Wu, X. Lu, G. Zheng, G.W. Ho, *Adv. Energy Mater.* **8**, 1702704 (2018)
- X. Sun, J. Huo, Y. Yang, L. Xu, S. Wang, *J. Energy Chem.* **26**, 1136–1139 (2017)
- Y. Yan, B.Y. Xia, B. Zhao, X. Wang, *J. Mater. Chem. A* **4**, 17587–17603 (2016)
- Y. Zheng, Y. Jiao, M. Jaroniec, S.Z. Qiao, *Angew. Chem. Int. Ed.* **54**, 52–65 (2015)
- Z.W. Seh, J. Kibsgaard, C.F. Dickens, I. Chorkendorff, J.K. Nørskov, T.F. Jaramillo, *Science* **355**, 6321 (2017)
- A. Wu, Y. Xie, H. Ma, C. Tian, Y. Gu, H. Yan, X. Zhang, G. Yang, H. Fu, *Nano Energy* **44**, 353–363 (2018)
- A.K. Sun, Y.L. Shen, Z.Z. Wu, D.Z. Wang, *Int. J. Hydrogen Energy* **42**, 14566–145719 (2017)
- W.C. Sheng, M. Myint, J.G. Chen, Y.S. Yan, *Energy Environ. Sci.* **6**, 1509 (2013)
- W. Zhang, Z. Yu, H.L. Jiang, S.H. Yu, *J. Am. Chem. Soc.* **136**, 14385–14388 (2014)
- P. Pachfule, D. Shinde, M. Majumder, Q. Xu, *Nat. Chem.* **8**, 718–724 (2016)
- J. Tang, R.R. Salunkhe, J. Liu, N.L. Torad, M. Imura, S. Furukawa, Y. Yamauchi, *J. Am. Chem. Soc.* **137**(4), 1572–1580 (2015)
- F.L. Wang, X.D. Yang, B.X. Dong, X. Yu, H.G. Xue, L.G. Feng, *Electrochem. Commun.* **92**, 33–38 (2018)
- X.S. Guo, Z.J. Feng, Z.Z. Lv, Y.F. Bu, Y.L. Liu, L.Q. Zhao, C.C. Hao, G.C. Li, Q.Q. Lei, *ChemElectroChem* **4**, 2052–2058 (2017)
- P.W. Menezes, A. Indra, C. Das, C. Walter, C. Göbel, V. Gutkin, D. Schmeißer, M. Driess, *ACS Catal.* **7**, 103–109 (2017)
- J. Ren, Z. Hu, C. Chen, Y.P. Liu, Z.Y. Yuan, *J. Energy Chem.* **26**, 1196–1202 (2017)
- Y.P. Zhu, Y.P. Liu, T.Z. Ren, Z.Y. Yuan, *Adv. Funct. Mater.* **25**, 7337–7347 (2015)
- J.T. Zhang, X. Liang, X.P. Wang, Z.B. Zhuang, *Mater. Lett.* **202**, 146–149 (2017)
- X. Liang, D.Z. Zhang, Z.Z. Wu, D.Z. Wang, *Appl. Catal. A* **524**, 134–138 (2016)
- Z.H. Pu, I.S. Amiinu, M. Wang, Y.S. Yang, S.C. Mu, *Nanoscale* **8**, 8500–8504 (2016)
- Y.F. Zhang, J. Yang, Q.C. Dong, H.B. Geng, Y. Zheng, Y.L. Liu, W.J. Wang, C.C. Li, X.C. Dong, *ACS. Appl. Mater. Interfaces* **10**, 26258–262639 (2018)
- J. Yang, F.J. Zhang, X. Wang, D.S. He, *Angew. Chem. Int. Ed.* **128**, 13046–13050 (2016)
- P. Liu, J.A. Rodriguez, *J. Am. Chem. Soc.* **127**, 14871–14878 (2005)
- R. Song, B. Luo, J.F. Geng, D.X. Song, D.W. Jing, *Ind. Eng. Chem. Res.* **57**, 7846–7854 (2018)

26. X.Y. Li, X. Qian, Y.L. Xu, H. Wu, Y.Y. Dan, L.Z. Chen, Q. Yu, *Electrochim. Acta* **321**, 134646 (2019)
27. K.L. Sun, K.H. Wang, T.P. Yu, X. Liu, G.X. Wang, L.H. Jiang, Y.Y. Bu, G.W. Xie, *Int. J. Hydrogen Energy* **44**, 1328–1335 (2019)
28. X.Z. Fang, L. Jiao, R. Zhang, H.L. Jiang, *A.C.S. Appl. Mater. Interfaces* **9**, 23852–23858 (2017)
29. R. Mo, S. Wang, H.X. Li, J. Li, S. Yang, J.X. Zhong, *Electrochim. Acta* **290**, 649–656 (2018)
30. Y.M. Du, Y. Han, X.D. Huai, Y.R. Liu, C.Y. Wu, Y. Yang, *Int. J. Hydrogen Energy* **43**, 22226–22234 (2018)
31. Y.M. Tian, J. Yu, H.S. Zhang, C. Wang, M.L. Zhang, Z.W. Lin, J. Wang, *Electrochim. Acta* **300**, 217–224 (2019)
32. X.P. Liu, S.F. Deng, D.D. Xiao, M.X. Gong, J.N. Liang, T.H. Zhao, T. Shen, D.L. Wang, *A.C.S. Appl. Mater. Interfaces* **11**, 42233–42242 (2019)
33. X.P. Yin, D. Lu, J.W. Wang, X.L. Lu, *ChemCatChem* **11**, 5407–5411 (2019)
34. K.W. Wang, J.S. Ten, Z.J. Lu, S. Chen, X.L. She, H.W. Zhang, D.J. Yang, *Int. J. Hydrogen Energy* **43**, 13939–13945 (2018)
35. Z. Wang, P. Ju, Y. Zhang, F.H. Jiang, H.B. Ding, C.J. Sun, *Electrochim. Acta* **187**, 424 (2020)
36. G.S. Song, S. Sun, Z.C. Wang, C.Z. Luo, C.X. Pan, *Acta Metall. Sin. (Engl. Lett.)* **30**, 1008–1016 (2017)
37. J. Zhao, Z.J. Yin, B.W. Wang, Z.H. Li, Y. Xu, X.B. Ma, *J. Energy Chem.* **47**, 248–255 (2020)
38. W.P. Xiao, L. Zhang, D. Bukhvalov, Z.P. Chen, Z.Y. Zou, L. Shang, X.F. Yang, D.Q. Yan, F.Y. Han, T.R. Zhang, *Nano Energy* **70**, 104445 (2020)
39. H.T. Du, L. Xia, S.Y. Zhu, F. Qu, F.L. Qu, *Chem. Commun.* **23**, 2854–2857 (2018)
40. E.H. Eladgham, D.D. Rodene, R. Sarkar, I.U. Arachchige, R.B. Gubta, *A.C.S. Appl. Nano Mater.* **3**, 8199–8207 (2020)
41. Y.D. Lu, Y.Y. Deng, S.L. Lu, Y.Y. Liu, J.P. Lang, X.Q. Cao, H.W. Gu, *Nanoscale* **11**, 21259–21265 (2019)
42. J. Yu, Q.Q. Li, Y. Li, C.Y. Xu, L. Zhen, V.P. Dravid, J.S. Wu, *Adv. Funct. Mater.* **26**, 7644–7651 (2016)
43. X.L. Yang, A.Y. Lu, Y.H. Zhu, M.N. Hedhili, S.X. Min, K.W. Huang, Y. Han, L.J. Li, *Nano Energy* **15**, 634–641 (2015)
44. C. Lin, Z.F. Gao, J.H. Yang, B. Liu, J. Jin, *J. Mater. Chem. A* **6**, 6387–6392 (2018)
45. Y.M. Du, M.J. Zhang, Z.C. Wang, Y.R. Liu, Y.J. Liu, Y.L. Geng, L. Wang, *J. Mater. Chem. A* **7**, 8602–8608 (2019)
46. P.P. Zhou, Y.Q. Zhang, B. Ye, S. Qin, R.R. Zhang, T.Y. Chen, H.J. Xu, L. Zheng, Q.H. Yang, *ChemCatChem* **11**, 6086–6091 (2019)
47. K.L. Yan, J.F. Qin, Z.Z. Lin, B. Dong, J.Q. Chi, W.K. Gao, J.H. Lin, Y.M. Chai, C.G. Liu, *Chem. Eng. J.* **334**, 922–931 (2018)
48. T.Y. Chen, R.R. Zhang, B. Ye, Q.H. Yang, H.J. Xu, L. Zheng, L.G. Wang, *Nanotechnology* **31**, 125402 (2020)
49. C. Wu, Y.J. Yang, D. Dong, Y.H. Zhang, J.H. Li, *Small* **13**, 1602873 (2017)
50. W. Zhang, J. Liang, L. Wang, Z.J. Feng, T.T. Yu, Z.H. Zhang, T.T. Yu, Z.H. Zhang, Y.L. Shao, C.C. Hao, G.C. Li, *Int. J. Hydrogen Energy* **43**, 2034–2042 (2018)

**Publisher's Note** Springer Nature remains neutral with regard to jurisdictional claims in published maps and institutional affiliations.